



Experimental and theoretical studies of reaction and growth of ultrathin Ni and Pd films on Al single crystal surfaces
by Vaithiyalingam Shutthanandan

A thesis submitted in partial fulfillment of the requirements for the degree of Doctor of Philosophy in Physics
Montana State University
© Copyright by Vaithiyalingam Shutthanandan (1994)

Abstract:

Reaction and growth of ultrathin Ni and Pd films, deposited on Al(110) and Al(001) surfaces at room temperature were studied using high-energy ion scattering, x-ray photoelectron spectroscopy, and x-ray photoelectron diffraction. For Ni deposited on Al(110) surfaces, a strong Ni-Al reaction occurs at the Ni-Al interface. For the first two monolayers (ML) of deposited Ni, a NiAl-like compound is formed. The reaction continues with a different rate, forming a Ni₃Al-like compound for Ni coverages from 2 to 8 ML, at which point a Ni metal film begins to grow on the interface. However, Ni atoms deposited at 250°C on the Al(110) surface, exhibit no surface compound formation, but diffuse 400 Å deep into the Al bulk.

Interatomic potentials based on the embedded atom method are used in a Monte Carlo approach to simulate the evolution of the Ni-Al(110) interface as a function of Ni coverage. The calculated ion scattering yields and x-ray photoelectron intensities from Ni and Al atoms in these simulated interfaces are in good quantitative agreement with the experimental results. The ion scattering simulations show that a large amount of near-surface dechanneling occurs just below the Ni-Al(110) interface.

In contrast to the Al(110) room temperature results, Ni deposited on the Al(001) surface under the same experimental conditions results in the growth of metastable body-centered-cubic Ni at the interface up to 5 ML of Ni coverage in a Stranski-Krastanov growth fashion. After the bcc islands coalesce to cover the surface, a disordered Ni metal film covers the interface.

Ultrathin Pd films deposited on Al(001) surfaces exhibit strong reaction at the Pd-Al(001) interface. For the first 5 ML of deposited Pd, a PdAl-like compound is formed. After 5 ML of Pd coverage, a Pd metal film covers the reacted interface.

EXPERIMENTAL AND THEORETICAL STUDIES OF REACTION
AND GROWTH OF ULTRATHIN Ni AND Pd FILMS ON
Al SINGLE CRYSTAL SURFACES

by

Vaithiyalingam Shutthanandan

A thesis submitted in partial fulfillment
of the requirements for the degree

of

Doctor of Philosophy

in

Physics

MONTANA STATE UNIVERSITY

Bozeman, Montana

May 1994

D378
Sh945

ii

APPROVAL

of a thesis submitted by

Vaithiyalingam Shutthanandan

This thesis has been read by each member of the thesis committee, and has been found to be satisfactory regarding content, English usage, format, citations, bibliographic style, and consistency, and is ready for submission to the College of Graduate Studies.

Apr 28 1994

Date

Richard J. Smith

Chairperson, Graduate Committee

Approved for the Physics Department

June 7, 1994

Date

J. Allen

Head, Physics Department

Approved for the College of Graduate Studies

6/22/94

Date

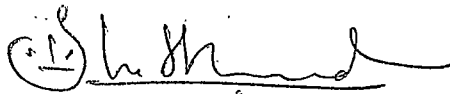
R. Brown

Graduate Dean

STATEMENT OF PERMISSION TO USE

In presenting this thesis in partial fulfillment of the requirements for a doctoral degree at Montana State University, I agree that the library shall make it available to borrowers under rules of the Library. I further agree that copying of this thesis is allowable only for scholarly purposes, consistent with "fair use as prescribed in the U.S. Copyright Law". Requests for extensive copying or reproduction of this thesis should be referred to University Microfilms International, 300 North Zeeb Road, Ann Arbor, Michigan 48106, to whom I have granted "the exclusive right to reproduce and distribute my dissertation for sale in and from microfilm or electronic format, along with the right to reproduce and distribute my abstract in any format in whole or in part."

Signature

A handwritten signature in black ink, appearing to be "D. H. H. H.", written over a horizontal line.

Date

6/15/94

To my wife **Janani**, whose patience, encouragement, and help have been beyond measure and generously given....

and

To my **mother** and late **father**, who have given their unqualified love, understanding, and support throughout my life.....

ACKNOWLEDGMENTS

I am very thankful to all the people in the Physics Department for their kindness and help during my graduate studies at Montana State University. My deepest gratitude goes to my advisor, Dr. Richard J. Smith, who guided me with continual support and encouragement. It has been a pleasure to work with Dr. Smith. Special thanks go to Dr. Adli Saleh for his continuous assistance and collaboration. Also I would like to thank N. R. Shivaparan for helping me with the Pd experiments. I would like to express my sincere thanks to N. Williams for his involvement in the design and construction of our wonderful sample holder, and his technical support, and E. Andersen for his technical assistance in the electronic field. Other people, who deserve a special mention, are Dr. J. Anderson and J. Pendyala.

I would also like to thank Dr. Art F. Voter from Los Alamos National Laboratory, Los Alamos, NM, for giving us his EAM potentials for Ni, Al, and Ni-Al alloys, and Dr. A. W. Denier van der Gon from Physics Department, Eindhoven University of Technology, Netherlands, for his helpful discussions about the EAM simulations.

I also acknowledge the financial support provided by the Physics Department and by the funds associated with the research grants of Dr. Smith. I appreciate the Physics Department for recognizing students from Sri-lanka and giving them an opportunity for graduate studies. Special thanks go to Dr. Robert Swenson, and Dr. John Hermanson in this respect. Finally, I would like to express gratitude to my wife, Janani, for her support during my years in the graduate school.

The work in this thesis was supported by the Montana Space Grant Consortium, NASA grant No. GT40041, and NSF EPSCOR No. RII-89211978 (MONT)

TABLE OF CONTENTS

	Page
ACKNOWLEDGMENTS.....	v
LIST OF TABLES.....	ix
LIST OF FIGURES.....	x
ABSTRACT.....	xv
1. INTRODUCTION.....	1
2. SHORT REVIEW OF THEORIES.....	6
Introduction.....	6
High energy ion scattering and channeling.....	6
Kinematic factor.....	8
Scattering cross section.....	9
Stopping cross section.....	10
Energy straggling.....	12
Quantitative analysis with RBS.....	12
Scattering yield.....	12
Channeling and shadowing.....	13
Surface structural information from channeling.....	17
Surface reconstruction.....	18
Surface relaxation.....	20
Growth of epitaxial overlayers.....	20
Interfacial reaction.....	21
X-ray photoelectron spectroscopy.....	21
Surface analysis with XPS.....	24
Element identification.....	24
Chemical shifts.....	24
Intensities and morphology.....	26
3. EXPERIMENTAL TECHNIQUES AND PROCEDURES.....	28
Introduction.....	28
Ultrahigh vacuum and UHV chamber.....	28
Ultrahigh vacuum.....	28
Ultrahigh vacuum chamber.....	31

High energy ion scattering experiment.....	33
Van de Graaff accelerator.....	33
Ion beam energies.....	34
Ion beam detection.....	35
Charge integration.....	36
Multichannel analyzer.....	37
Goniometer and sample holder.....	38
X-ray photoelectron spectroscopy.....	40
X-ray source.....	41
Hemispherical analyzer.....	42
Electron multipliers.....	45
Sample preparation.....	46
Orientation of the surface.....	46
Fine polishing.....	47
Cleaning in vacuum.....	48
Thin film deposition.....	51
Locating the channeling direction.....	52
4. MONTE CARLO SIMULATIONS AND EMBEDDED ATOM METHOD POTENTIALS.....	54
Introduction.....	54
Ion scattering simulations.....	56
Embedded atom method and potentials.....	60
Bulk simulation.....	64
Simulation of Al(110) surface.....	66
Simulation of Ni on Al(110) Surface.....	75
5. ULTRATHIN Ni FILMS ON Al(110) SURFACES.....	82
Introduction.....	82
Experimental setup.....	83
Results and discussion.....	85
Ni deposition onto Al(110) at room temperature.....	85
High energy ion scattering and channeling.....	85
High energy ion scattering simulation.....	93
X-ray photoelectron spectroscopy.....	100
XPS intensity simulation.....	112
Exploring the snapshots.....	118
Slow deposition of Ni.....	128
Ni deposition onto Al(110) @ 250°C.....	132

6. ULTRATHIN Ni FILMS ON Al(001) SURFACES.....	142
Introduction.....	142
Experimental setup.....	143
Results.....	145
High energy ion scattering.....	145
X-ray photoelectron spectroscopy.....	150
Photoelectron diffraction.....	154
Discussion.....	160
7. ULTRATHIN Pd FILMS ON Al(001) SURFACES.....	174
Introduction.....	174
Experimental setup.....	175
Results.....	176
High energy ion scattering.....	176
X-ray photoelectron spectroscopy.....	179
Discussion.....	180
8. CONCLUSION.....	189
REFERENCES.....	192
APPENDICES.....	198
Appendix I XPS curve fitting.....	199
Appendix II Sample holder design.....	201
Appendix III EAM and MC Program description.....	207

LIST OF TABLES

Table		Page
I	Optimized EAM potential parameters.....	62
II	Comparison of the multilayer relaxation between simulation and experiment.....	68
III	Comparison of chemical shifts and satellite separation for the Ni $2p_{3/2}$ peak in different Ni-Al alloys.....	107
IV	Comparison of different structural properties of Al, Ni, NiAl, and Ni ₃ Al alloys.....	124
V	Comparison of chemical shifts and satellite separation for the Pd 3d peaks in different Pd-Al alloys.....	184

LIST OF FIGURES

Figure	Page
2.1 Schematic of Rutherford backscattering spectroscopy.....	7
2.2 Comparison between the channeling spectrum and the random spectrum for He ⁺ ions backscattering from Al(110) surface.....	14
2.3 Shadowing effect and the formation of the shadow cone.....	15
2.4 Different uses of ion scattering technique.....	19
2.5 Schematic of X-ray photoelectron spectroscopy.....	23
2.6 XPS spectrum from a Ti alloy.....	25
2.7 XPS spectrum from 12 ML Ni film deposited on Al surface.....	26
3.1 Schematic diagram of the side view of the UHV chamber.....	29
3.2 Schematic diagram of the top view of the UHV chamber.....	30
3.3 Schematic drawing of the Van de Graaff accelerator and the beam line.....	31
3.4 Outline drawing of the multichannel analyzer-detector setup.....	38
3.5 Schematic drawing of the different motions of the goniometer.....	39
3.6 Schematic diagram of the basic components of the x-ray photoelectron spectrometer (XPS).....	42
3.7 The Laue x-ray diffraction pattern from Al (110) single-crystal surface.....	46
3.8 Al 2p XPS spectrum for dirty and clean Al surfaces.....	50
4.1 Schematic flow diagram of Metropolis scheme in MC simulations.....	56
4.2 Functional forms of the EAM potentials.....	59

4.3	Acceptance ratio in the Al bulk simulations as a function of step size.....	65
4.4	Snapshots of simulated Al(110) surface for different coverage of Ni.....	67
4.5	Multilayer relaxation in Al(110) surfaces.....	69
4.6	Calculated Al ion scattering yield as a function of delta.....	71
4.7	Flow diagram of the "thin-thick" approach.....	72
4.8	Calculated Al ion scattering yield for 1 MeV He ions versus number of MC cycles.....	73
4.9	Calculated ion scattering yield from each layer in the clean Al(110).....	75
4.10	Flow diagram showing the Ni on Al(110) simulation procedure....	77
4.11	Calculated Al ion scattering yield and the total energy of the crystal as a function of number of MC cycles.....	78
4.12	Number of atoms in a layer as a function of total number of MC cycles.....	79
4.13	Layer definition in the MC simulation.....	80
5.1	ion scattering spectra for 1 MeV He ⁺ ions on Ni+Al(110) for different Ni coverages.....	87
5.2	Measured ion scattering yield from Ni atoms on Al(110) surface as a function of deposition time.....	88
5.3	Number of Ni atoms visible to the ion beam as a function of Ni coverage.....	89
5.4	Number of Al atoms visible to the ion beam as a function of Ni coverage.....	91
5.5	Measured and simulated ion scattering yields from Al atoms as a function of Ni coverage.....	94

5.6	Measured and simulated ion scattering yields from Ni atoms as a function of Ni coverage.....	95
5.7	Extra-simulated ion scattering yield from Al atoms in each layer.....	97
5.8	Ni $2p_{3/2}$ XPS spectra for selected Ni coverages.....	101
5.9	Average chemical shift of Ni 2p line and satellite separation from Ni $2p_{3/2}$ line as a function of Ni coverage.....	105
5.10	Measured XPS intensity of Al 2p and Ni $2p_{3/2}$ as a function of Ni coverage.....	109
5.11	Schematic of the coordinate system of the EAM simulated snapshots used for the XPS intensity calculation.....	113
5.12	Simulated XPS intensities of Ni 2p line for different values of λ	115
5.13	Simulated and measured XPS intensities of Al 2p and Ni 2p as a function of Ni coverage.....	117
5.14	Normalized layer occupancies of Al, Ni and total atoms as a function of Ni coverage.....	119
5.15	Top view of the snapshot of the simulated Al(110) surface for two different coverage of Ni.....	122
5.16	Average nearest neighbor distance of atoms in each layer as a function of Ni coverage.....	126
5.17	Number of Al atoms visible to the ion beam as a function of Ni coverage for two different deposition rates of Ni.....	129
5.18	Ion scattering spectra for 1.7 Ml of Ni deposited on the Al(110) surface at different temperatures.....	133
5.19	Ion scattering spectra for Ni on Al(110) at 250°C for different Ni coverages.....	135
5.20	Channeling and random spectra of 4.8 Ml of Ni on Al(110) at 250°C.....	136

5.21	Concentration profile of Ni on Al(110) at 250°C.....	137
5.22	Measured XPS intensities of Al 2p and Ni 2p _{3/2} as a function of Ni coverage at 250° C.....	138
6.1	Backscattered ion energy spectra for 0.97 MeV He ions on Ni+Al(001) for different Ni coverages.....	146
6.2	Number of Al atoms visible to the ion beam as a function of Ni coverage on Al(001) surfaces.....	147
6.3	Number of Ni atoms visible to the ion beam as a function of Ni coverage on Al(001) surfaces.....	148
6.4	Surface peak position of Al as a function of Ni coverage.....	149
6.5	Ni 2p _{3/2} XPS spectra from Ni+Al(001) surface for selected Ni coverage.....	151
6.6	Average chemical shift of Ni 2p line and satellite separation from the Ni 2p _{3/2} line as a function of Ni coverage.....	152
6.7	Measured XPS intensity of Al 2p and Ni 2p _{3/2} as a function of Ni coverage.....	153
6.8	Al 2p polar XPD scan for clean Al(001) surface in (110), and (010) azimuthal planes.....	155
6.9	Ni 3p polar XPD scan for several coverages of Ni in the (110) azimuthal plane.....	156
6.10	Ni 3p polar XPD scan for several coverages of Ni in the (010) azimuthal plane.....	157
6.11	Al 2p polar XPD scan for several coverages of Ni in the (110) azimuthal plane.....	158
6.12	Al 2p polar XPD scan for several coverages of Ni in the (010) azimuthal plane.....	159
6.13	Total energy of the Al(001) slab with 1 Ni atom calculated using EAM potentials.....	163

6.14	Expected forward focusing peaks in the polar scan of bcc and fcc structures for different azimuthal planes.....	165
6.15	Background corrected Ni XPD polar scans in the (110) and (010) azimuths.....	170
7.1	Ion scattering spectrum for 1 MeV He ions on Pd+Al(001) for different Pd coverage.....	177
7.2	Number of Al atoms visible to the ion beam as a function of Pd coverage.....	178
7.3	Number of Pd atoms visible to the ion beam as a function of Pd coverage.....	179
7.4	Pd 3d XPS spectra from Pd films on Al(001) surfaces for different Pd coverages.....	182
7.5	Measured XPS intensities from Pd 3d _{5/2} as a function of Pd coverage.....	185
7.6	Corrected XPS intensities from Pd 3d _{5/2}	186

ABSTRACT

Reaction and growth of ultrathin Ni and Pd films, deposited on Al(110) and Al(001) surfaces at room temperature were studied using high-energy ion scattering, x-ray photoelectron spectroscopy, and x-ray photoelectron diffraction. For Ni deposited on Al(110) surfaces, a *strong Ni-Al reaction* occurs at the Ni-Al interface. For the first two monolayers (ML) of deposited Ni, a NiAl-like compound is formed. The reaction continues with a different rate, forming a Ni₃Al-like compound for Ni coverages from 2 to 8 ML, at which point a Ni metal film begins to grow on the interface. However, Ni atoms deposited at 250°C on the Al(110) surface, exhibit no surface compound formation, but diffuse 400 Å deep into the Al bulk.

Interatomic potentials based on the embedded atom method are used in a Monte Carlo approach to simulate the evolution of the Ni-Al(110) interface as a function of Ni coverage. The calculated ion scattering yields and x-ray photoelectron intensities from Ni and Al atoms in these simulated interfaces are in good quantitative agreement with the experimental results. The ion scattering simulations show that a large amount of *near-surface dechanneling* occurs just below the Ni-Al(110) interface.

In contrast to the Al(110) room temperature results, Ni deposited on the Al(001) surface under the same experimental conditions results in the growth of metastable *body-centered-cubic* Ni at the interface up to 5 ML of Ni coverage in a Stranski-Krastanov growth fashion. After the *bcc* islands coalesce to cover the surface, a disordered Ni metal film covers the interface.

Ultrathin Pd films deposited on Al(001) surfaces exhibit *strong reaction* at the Pd-Al(001) interface. For the first 5 ML of deposited Pd, a PdAl-like compound is formed. After 5 ML of Pd coverage, a Pd metal film covers the reacted interface.

CHAPTER 1

INTRODUCTION

Ultrathin films of metals on metal substrates have been the subject of intense interest in recent years. In particular, a considerable amount of interest has been focused on trying to understand the interface structures and growth modes of these systems, which range from reaction¹, to island growth², to epitaxial growth³. Generally, the growth modes of vapor-deposited thin films are categorized into the following groups: (1) Frank-van der Merwe (monolayer-by-monolayer growth, FM mode), (2) Stranski-Krastanov (layer growth up to one or a few monolayers, followed by three-dimensional island growth, SK mode), (3) Volmer-Weber (formation of three-dimensional islands, VW mode), (4) Compound formation (formation of a surface alloy as a result of reaction between the adsorbate and the substrate). The driving force in these growth modes is the minimization of the total energy of the system. The total energy includes surface energy of the substrate and adsorbate, and the interfacial energy⁴. The surface energies of a particular substrate and the adsorbate can be calculated or obtained experimentally, but the interfacial energy cannot be determined easily, since strong reaction between the adsorbate and substrate can complicate the matter.

We have focused our studies on transition-metal aluminum interfaces because of their technological applications⁵ as well as the fundamental interest discussed

above. Aluminum-based transition metal alloys are important in applications for catalysis, high-temperature, low-density structural materials⁵, and metalization layers in semiconductors⁶. Also, thin films of transition metal aluminides may have different physical properties than those of the bulk material since the electronic and atomic structures in the overlayer may also be modified.

This thesis work is part of a systematic investigation to understand the fundamentals which determine the growth modes of ultrathin transition-metal films deposited on Al single-crystal substrates. In this study, we mainly concentrated on Ni and Pd ultrathin films on different Al single-crystal surfaces. A detailed description of the structures and growth modes of some other transition metal overlayers, namely Ti/Al and Fe/Al, is given elsewhere^{3,7}.

There have been numerous studies of the Ni-Al system at elevated temperature, including X-ray diffraction (XRD)⁸, photoemission spectroscopy⁹, Rutherford backscattering spectroscopy (RBS)¹⁰, ion beam mixing¹¹, transmission electron microscopy (TEM)¹², and glancing angle x-ray diffraction¹³. Of these, only the TEM work was performed on Al single-crystal surfaces. The remaining experiments were performed either on polycrystalline substrates or on bilayers of Ni and Al. Not all of the results from these experiments are in agreement, but most of them suggest that there is a strong reaction between the Ni and Al atoms, and that NiAl₃ is the first phase to form at the Ni/Al interface at elevated temperatures. For the photoemission and glancing angle x-ray experiments, room-temperature reaction was reported. Because of these conflicting observation, the Ni-Al system merits more attention.

The study of ultrathin Pd films on Al single-crystal surfaces is also very interesting since Ni and Pd have similar bulk equilibrium phase diagrams as Al¹⁴, and they belong to the same group in the periodic table. Because of these similarities, we might expect the behavior of Pd on Al single-crystal surfaces to be similar to that for the Ni-Al system. Like Ni-Al, some conflicting results have been reported for the Pd-Al system in the past^{1,15}.

In this thesis work we explored the growth and reaction of ultrathin Ni and Pd films on Al(110) and Al(001) surfaces. During the growth process the atomic and the electronic structures of the overlayer and the substrate were monitored with different surface science techniques. The experimental techniques which we used in this work are high-energy ion scattering (HEIS), x-ray photoelectron spectroscopy (XPS), and x-ray photoelectron diffraction (XPD). The HEIS and XPD techniques are primarily used to characterize the interface structure, while XPS is used to identify the chemical state of the interface. In Chapter 2, the basic theory of the aforementioned experiments are briefly reviewed. The experimental setups and procedures are discussed in detail in Chapter 3. In Chapter 5, the results of ultrathin Ni films deposited on Al(110) surfaces using HEIS and XPS are reported. The HEIS, XPS, and XPD experimental results of ultrathin Ni films on Al(001) surfaces are discussed in Chapter 6, while Pd films deposited on the Al(001) surface are discussed in Chapter 7.

The aforementioned experimental investigations are often aided by complementary theoretical work, especially in the HEIS case¹⁶. In this study we

developed a new approach to simulate our ion scattering yield and XPS intensity results. In this approach we determine the positions of the atoms as they evolve in a Monte Carlo (MC) simulation¹⁷. The interactions between the atoms are calculated using Embedded-Atom-Method (EAM) potentials¹⁸. Snapshots of the evolving interface are then generated and used to calculate the ion scattering and photoelectron yields. These simulated yields are then compared quantitatively with the experimentally observed results. The EAM potential used in these calculations and the procedures used to simulate the interface are discussed in Chapter 4. The results of the simulations of ultrathin Ni films on Al(110) surfaces are discussed together with the experimental results in Chapter 5.

Some of the acronyms that are frequently used in this thesis are listed below.

AES	Auger electron spectroscopy
EAM	Embedded atom method
FAT	Fixed-analyzer transmission
FM	Frank-van der Merwe
FWHM	Full width at half maximum
HEIS	High energy ion scattering
HA	Hemispherical analyzer
MC	Monte Carlo
MCA	Multichannel analyzer
ML	Monolayer
MCS	Multichannel scaling

PIPS	Passivated, implanted, planner silicon detector
PHA	Pulse height analysis
RBS	Rutherford backscattering spectroscopy
RGAs	Residual gas analyzer
SPA	Surface peak area
SK	Stranski-Krastanov
UHV	Ultra-high vacuum
VEGAS	Ion scattering simulation program
VW	Volmer-Weber
XPS	X-ray photoelectron spectroscopy
XPD	X-ray photoelectron diffraction

CHAPTER 2

SHORT REVIEW OF THEORIESIntroduction

The experimental techniques used in this thesis work are high-energy ion scattering (HEIS), channeling and x-ray photoelectron spectroscopy (XPS). The main work has been the measurement of surface peak area (SPA) of the substrate (Al) and the adsorbate (Ni and Pd) in HEIS at different adsorbate coverages in order to investigate the reaction and growth modes of ultrathin transition metals films deposited on Al-single crystal surfaces. Furthermore, HEIS was used to measure the actual coverage of the adsorbate (Ni or Pd). In addition, XPS measurements have been performed to identify the chemical state of the reacted transition metal-Al interface during the Ni (or Pd) deposition. In this Chapter we give a short description of physical concepts and the theory behind these powerful surface science techniques. In the next chapter we will discuss the instrumentation and the experimental details of these methods.

High-energy Ion Scattering and Channeling

Rutherford backscattering spectroscopy (RBS) is a commonly used, non-destructive, surface analysis probe in modern physics¹⁹. The basic idea behind RBS is

very simple. A beam of energetic ions (He^+ , H^+) is directed at the surface of the sample. The ions interact elastically with atoms in the sample and are backscattered into a solid-state detector which counts the number of particles according to their energy. From the energy spectrum of backscattered ions we can infer considerable structural information about the sample, such as the thickness, average composition, and quality of the sample. In particular, if we align the incident ion beam along a low-index crystallographic direction in a single crystal sample, we can achieve substantial surface sensitivity, depending on the incident energy.

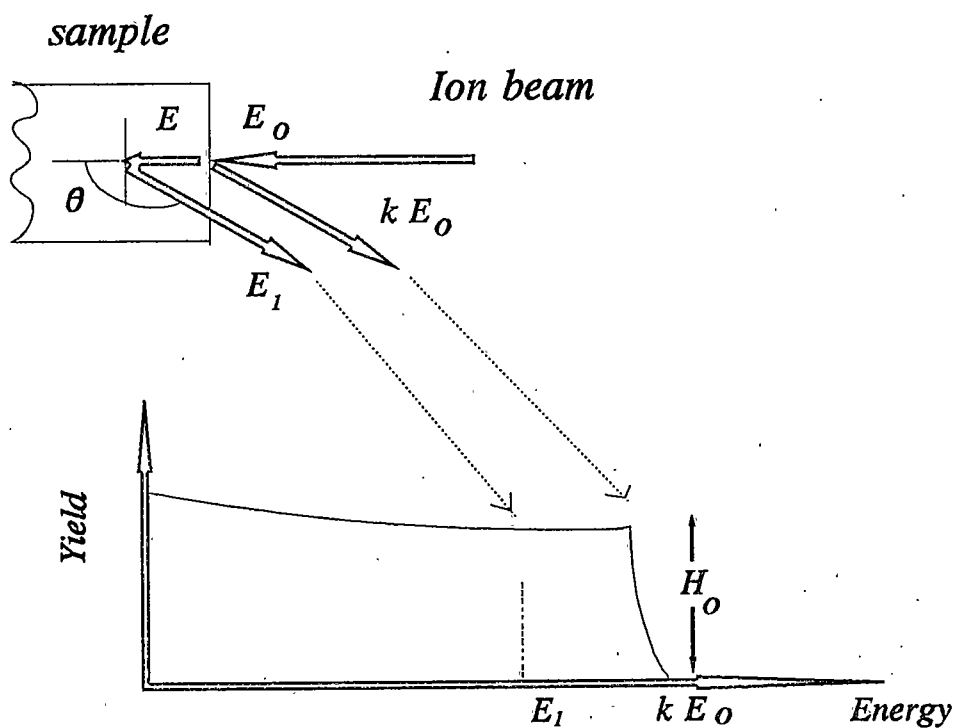


Figure 2.1: Schematic of Rutherford backscattering spectroscopy (RBS)

A typical RBS spectrum from a single-element target is shown in Figure 2.1, where the beam of energetic ions with energy E_0 , mass M_1 , and charge Z_1 strikes the sample (with atomic mass M_2 , and charge Z_2) at normal incidence, and backscattered ions are detected at a scattering angle θ . While a small fraction of the beam scatters from the surface atoms, additional scattering occurs from the atoms just below the surface. In moving through a sample before the scattering encounter, and passing back out through the sample after the scattering event, the ions continue to lose energy. The ions scattered from the surface atoms will reach the detector with energy KE_0 , where K is a constant less than unity, whereas the ions scattered from the atoms which are below the surface will give signals at energies less than KE_0 , as shown in Figure 2.1. The four basic physical properties which govern the RBS process are¹⁹: (1) *kinematic factor* K - used for mass determination, (2) *stopping cross section* - useful for depth analysis, (3) *scattering cross section* - important for quantitative analysis, (4) *energy straggling* - limits the mass and energy resolution. In the following paragraphs, we briefly describe the aforementioned concepts of RBS.

Kinematic factor K

Consider the geometry in Figure 2.1, which illustrates the scattering of energetic ions from a single-element target. The energy of the ions backscattered from the surface atoms can be related to the incident energy via the kinematic factor K , as¹⁹

$$E_s = K E_o \quad (2.1)$$

where K is given by

$$K = \left[\frac{M_1 \cos\theta + (M_2^2 - M_1^2 \sin^2\theta)^{1/2}}{(M_1 + M_2)} \right]^2 \quad (2.2)$$

Equation 2.2 shows that the kinematic factor depends only on the masses M_1 , and M_2 , and the lab scattering angle θ .

Scattering cross section $d\sigma/d\Omega$

The probability of the scattering event to occur as illustrated in Figure 2.1 depends on the average scattering cross section (σ). The detector subtends a solid angle Ω about the scattering direction, θ . Then, for a small Ω , the average scattering cross section can be approximated being the differential scattering cross section $d\sigma/d\Omega$. Furthermore, if the interaction between the ions and the atoms is specified by the Moliere potential²⁰, then the differential scattering cross section is given by²¹

$$\frac{d\sigma}{d\Omega} = F \left[\frac{Z_1 Z_2 e^2}{2E_0 \sin^2 \theta} \right]^2 \frac{\left[\left(1 - \left[\frac{M_1}{M_2} \sin \theta \right]^2 \right)^{\frac{1}{2}} + \cos \theta \right]^2}{\left[1 - \left[\frac{M_1}{M_2} \sin \theta \right]^2 \right]^{\frac{1}{2}}} \quad (2.3)$$

where F is a screening correction factor

$$F = 1 - \frac{0.042 Z_1 Z_2^3}{E(\text{keV})} \quad (2.4)$$

Stopping cross section

As we mentioned earlier, when an energetic ion passes through a solid it loses energy (dE/dx) through electronic interactions. If we consider these energy losses in the solid for the ingoing and outgoing ions, then the energy difference ΔE , between ions scattered from the surface and ions scattered at a depth x from the surface, is given by ¹⁹

$$\Delta E = x \left[\frac{K}{\cos \theta_1} \frac{dE}{dx} \Big|_{E_0} + \frac{1}{\cos \theta_2} \frac{dE}{dx} \Big|_{KE_0} \right] \quad (2.5)$$

where θ_1 is defined as the angle between the surface normal of the sample and the

direction of the incident ions, and θ_2 is defined as the angle between the normal direction and the direction of backscattered ions. For normal incidence, $\theta_1 = 0^\circ$, and $\theta_2 = 180^\circ - \theta$, where θ is the scattering angle in the laboratory. Usually, the energy loss dE/dx is related to the stopping cross section ϵ by the following Equation

$$\frac{dE}{dx} = \epsilon N \quad (2.6)$$

where N is the atomic density of the target atoms.

Using Equation 2.5 and 2.6, we can convert the energy-difference Equation into a depth Equation¹⁹, that is

$$\Delta E = N x [\epsilon] \quad (2.7)$$

with

$$[\epsilon] = \left[\frac{K}{\cos\theta_1} \epsilon(E_o) + \frac{1}{\cos\theta_2} \epsilon(KE_o) \right] \quad (2.8)$$

where $\epsilon(E_o)$ and $\epsilon(KE_o)$ are evaluated at energy E_o and KE_o , respectively.

Energy Straggling

The energy-loss process which we discussed in the previous section is subject to statistical fluctuations. As a result of these fluctuations, identical ions passing through the same distance inside the solid may have different energies as they leave from the sample. The energy loss due to this fluctuation is referred to as energy straggling¹⁹. Moreover, any uncertainty in the ion energy due to the straggling will affect the mass and depth resolution in RBS.

Quantitative analysis with RBS

Scattering Yield

In general, the ion scattering yield (Y) from a single-element target is given by¹⁹

$$Y = Q N t \frac{d\sigma}{d\Omega} \Omega \quad (2.9)$$

where

Q is the number of incident ions at the target,

N is the volume density of the target atoms,

t is the thickness of the sample,

$d\sigma/d\Omega$ is the differential scattering cross section, and

Ω is the solid angle subtended by the detector.

For the example illustrated in Figure 2.1, the ion scattering yield in the surface region is equal to the height (H_o) of the spectrum, and is given by¹⁹

$$H_o = \frac{d\sigma(E_o)}{d\Omega} \Omega Q \frac{\delta E}{[E_o]} \quad (2.10)$$

where δE is the energy loss associated with thickness t of the sample, and is typically the energy width of a single channel in the spectrum. The other parameters are the same as before.

Channeling and Shadowing

When the ion beam is well aligned with a low-index crystallographic direction of the single crystal, the ions channel through the crystal along the relatively open areas between the rows of atoms²⁰. Channeled ions do not make close-encounter collisions with the substrate target atoms. Hence the RBS yield is reduced at all depths as seen in Figure 2.2, where the aligned spectrum and the random-direction spectrum from an Al(110) crystal are shown. Roughly 95% of the incident ions are channeled through the crystal. Furthermore, shadowing of the underlying atoms by the surface atoms as shown in Figure 2.3 will reduce the RBS yield. This reduced RBS yield is referred to as aligned yield. Due to the limitations of depth resolution, the aligned yield

will show a small *surface peak* (SP), spread over the first few channels of the spectrum²⁰. If the incident ion beam is not aligned with a low-index direction, the RBS yield will be that for a random distribution of target atoms, i.e. the spectrum (Figure 2.2) will look like the one we described in Figure 2.1. The yield collected in the random direction is referred to as *the random yield*.

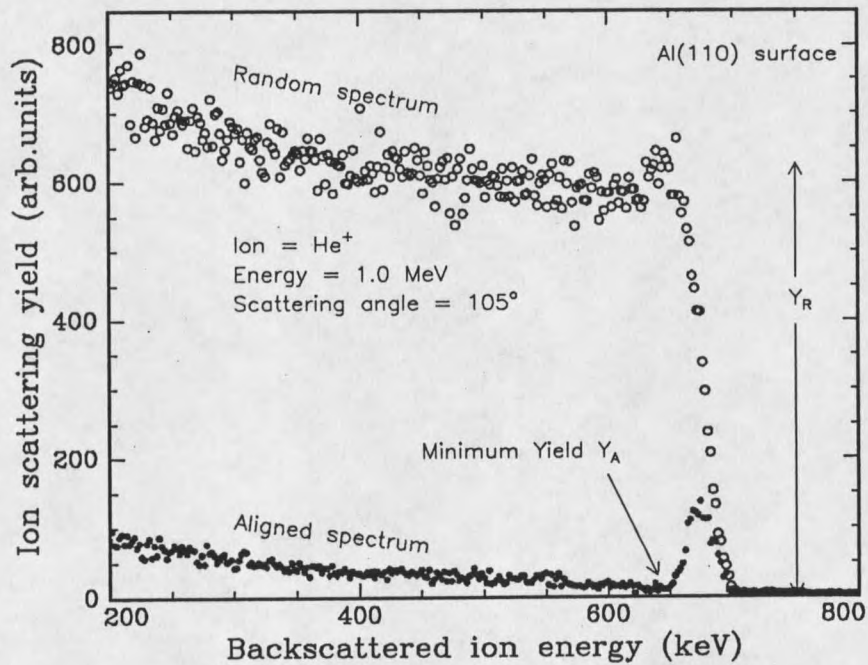


Figure 2.2 : Comparison between the channeling spectrum (closed circles) and the random spectrum (open circles) for He⁺ ions backscattering from the Al(110) surface.

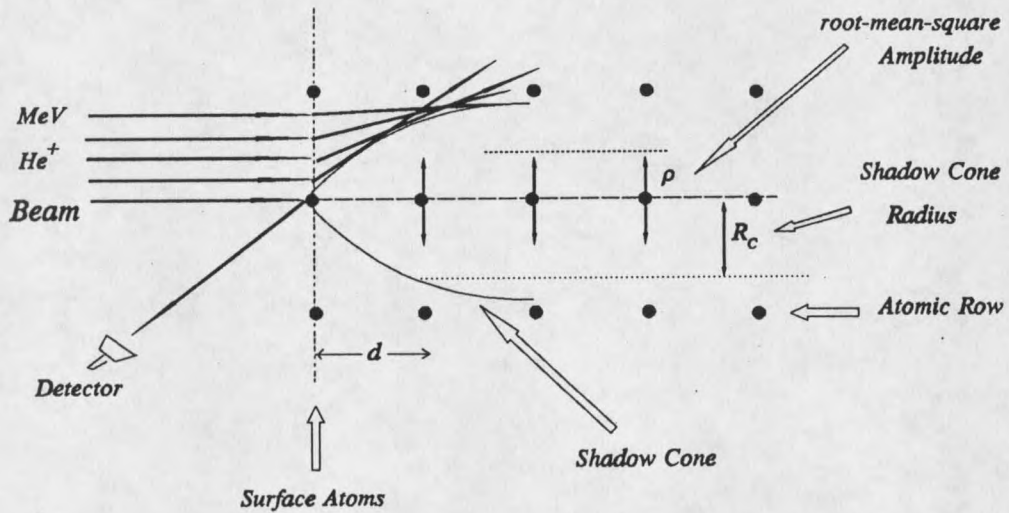


Figure 2.3 : Shadowing effect and the formation of the shadow cone in an ideal crystal.

While the surface peak is a measure of *surface order*, the minimum yield behind the surface peak (Figure 2.2) is a measure of the *bulk crystal perfection*^{19,20}. Furthermore, a measure of the channeling effect is the quantity χ_{\min} , where χ_{\min} is defined as the ratio of the aligned to random yield¹⁹, i.e., $\chi_{\min} = Y_A/Y_R$ (see Figure 2.2). A smaller value of χ_{\min} corresponds to better channeling. This minimum yield, χ_{\min} , can be calculated from the relation¹⁹

$$\chi_{\min} \approx N d \pi (2u_1^2 + a^2) \quad (2.11)$$

where N is the atomic density, u_1 is the atomic one-dimensional vibrational amplitude, d is the interatomic distance along the row, and a is the Thomas-Fermi screening radius. Values of χ_{\min} are typically between 0.01 and 0.04.

In a channeling experiment the ions which backscatter from the first atoms in each row give rise to the surface peak observed in the energy distribution spectrum of backscattered ions (Figure 2.2), while the small-angle forward-scattered ions form a "shadow cone" with radius R_c , which extends into the solid (see Figure 2.3). For a Coulomb potential the shadow cone radius is given by²⁰

$$R_c = 2 \sqrt{\frac{Z_1 Z_2 e^2 d}{E}} \quad (2.12)$$

In Figure 2.2, the surface peak area (SPA) is a direct measure of how many surface atoms are visible to the incident ion beam. For the channeling case, the scattering yield Y in Equation 2.9 will be the surface peak area. Thus, if we know the SPA, Q , Ω and the scattering cross section, then by using Equation 2.9 we can calculate the product Nt , the *number of atoms per unit area* visible to the beam.

For a static model of an ideally terminated bulk lattice, subsequent atoms along the row and within the shadow cone do not lead to backscattered ions. However, at room temperature atoms vibrate with the two-dimensional root-mean-square

